Inertial gyre solutions from a primitive equation ocean model

by Annalisa Griffa[1], Eric P. Chassignet[1], Victoria Coles[1] and Donald B. Olson[1]

ABSTRACT

A numerical exploration of inertial equilibrium states obtained with a primitive equation ocean model suggests that they can be described using statistical mechanics theory developed in the framework of quasi-geostrophy. The performance of the numerical model is first assessed with respect to the quasi-geostrophic model considering a series of experiments in the quasi-geostrophic range, in a closed basin with flat bottom and varying Rossby numbers. The results show that our model is consistent with the quasi-geostrophic model even in terms of dependence from boundary conditions and eddy viscosity values, and that the free surface contribution is negligible. As in the quasi-geostrophic experiments, a tendency toward Fofonoff flows is observed. This tendency remains in a second series of experiments performed outside the quasi-geostrophic range, namely with flows with higher Rossby numbers and with steep topography, characterized by sloping boundaries with an order one fractional change in the depth. It is only close to the boundaries that ageostrophic effects modify the flows. In conclusion, the fact that statistical mechanics theory, initially developed in the framework of quasi-geostrophy, holds for more realistic flows with steep topography supports development of subgrid scale parameterizations based on statistical mechanics theory, to be used in realistic general circulation models.

1. Introduction

The inertial characteristics of the oceanic circulation in a closed basin have been extensively discussed in the literature. In particular, the purely inertial limit (i.e., the limit of no forcing and no dissipation) for quasi-geostrophic flows has been studied using the theory of statistical mechanics. This theory predicts the existence of inertial equilibrium states corresponding to the maximum entropy of the system, characterized by mean flows with a linear relationship between stream function and potential vorticity (Salmon *et al.,* 1976). These flows are often called "Fofonoff flows" because, in the case of a one layer, flat bottom, β-plane basin, they correspond to the well known two-gyre solutions of the steady quasi-geostrophic equation first studied by Fofonoff (1954). In the presence of topography, the Fofonoff flows are modified and are given by solutions locked to the topography (Carnevale and Frederiksen, 1987). These Fofonoff states have also been shown to be relevant in the evolution of inertial flows by another independent theory, valid for weakly dissipative flows and based on the idea of enstrophy minimization (Bretherton and Haidvogel, 1976).

---

1. RSMAS/MPO, University of Miami, 4600 Rickenbacker Causeway, Miami, Florida, 33149, U.S.A.

The predictions of the theory of statistical mechanics, and in particular the emergence of mean Fofonoff flows, have been tested in a number of numerical studies using the quasi-geostrophic equation. Purely inertial solutions and weakly dissipative ones have been studied in "initial release" experiments, where an initial random field of eddies is allowed to evolve freely and the emergence of equilibrium solutions is observed. The results show good agreement with the theory (e.g., Wang and Vallis, 1994; Cummins and Holloway, 1994; referred to as WV and CH respectively hereafter). A number of experiments have also been performed with forcing and dissipation to study the relevance of the inertial equilibrium states to forced solutions. In these experiments, Fofonoff flows, despite the presence of forcing, appear to be representative of the tendency of the nonlinearity, and the actual shape of the forced solutions depends on the competition between this tendency and the effects of the forcing (e.g., Griffa and Salmon, 1989; Cummins, 1992, referred to as GS and C92 respectively hereafter; Griffa and Castellari, 1991).

An interesting question, still open in the literature, is whether or not the inertial tendency toward the Fofonoff flows persists outside the range of validity of quasi-geostrophy. This question is not a simple one to address theoretically, as generalizations of statistical mechanics theories are difficult to achieve. They have been attempted only for some specific cases (e.g., Salmon, 1982a; Errico, 1984). Until now, the numerical experiments for oceanic flows have been performed with the quasi-geostrophic equation only.

As suggested by Holloway (1992), the validity of the statistical mechanics theory outside quasi-geostrophy can have important and practical consequences. If the tendency toward a Fofonoff flow survives within the range of validity of the primitive equations, and if it is characteristic of the nonlinearity, it can then be used as a basis for a new and more accurate parameterization of the actions of subgrid scale nonlinear effects in low resolution ocean general circulation models (OGCMs). The parameterization proposed by Holloway (1992) would replace the traditional eddy viscosity that tends to drive the flow toward a state of rest with a term which would drive the barotropic part of the solution toward a Fofonoff flow (Alvarez *et al.,* 1994; Eby and Holloway, 1994).

This paper reflects a first step in the direction of studying the inertial characteristics of the solutions using the primitive equations. In particular, it addresses the question as to whether the tendency toward the Fofonoff flow remains. A one-layer shallow water numerical model (Bleck and Boudra, 1986) is used to analyze the primitive equation solutions in a β-plane basin, with no forcing and with weak or no dissipation. First, a set of flat-bottom solutions within the quasi-geostrophic regime is compared to previously obtained quasi-geostrophic results (GS, C92, WV). The importance of the dissipation operator and of the boundary conditions used in the numerical model are investigated. Solutions outside the quasi-geostrophic range are then presented to study the effects of steep topography and stronger nonlinearity on the tendency toward Fofonoff flows.

The layout of the paper is the following. In Section 2, the application of statistical mechanics and its limitations are reviewed. In Section 3, the characteristics of the numerical model are presented, and in Section 4, the parameters of the numerical
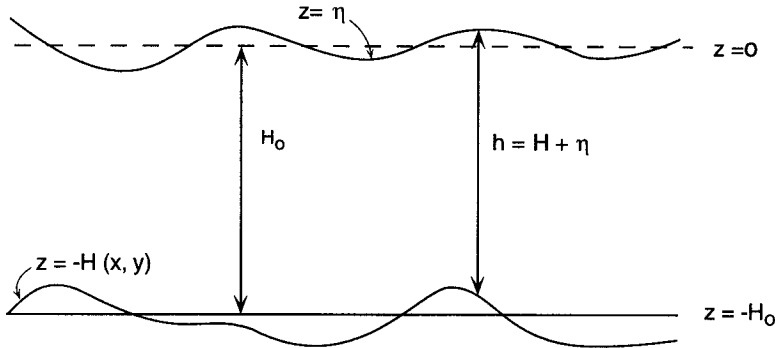
Figure 1. Schematic representation of the one-layer shallow water model.

experiments are introduced. The experiments with flat bottom and steep topography are discussed in detail in Sections 5 and 6, respectively. Finally, the results are summarized and discussed in the concluding section.

2. Background

a. Equilibrium statistical mechanics and quasi-geostrophy. The theory of equilibrium statistical mechanics applies to the quasi-geostrophic equation in the limit of no forcing and no dissipation (e.g., Holloway, 1986). The one-layer quasi-geostrophic equation with the rigid lid approximation and under these constraints is

$$\partial q/\partial t + J(\psi, q) = 0 \qquad (1)$$

where $q = \zeta + f + h^*$ is the absolute vorticity, $\zeta = \nabla^2\psi$ is the relative vorticity, ψ is the stream function, $f = f_0 + \beta y$ is the Coriolis parameter, and $h^* = -f_0 H/H_0$ is the topographic function with $H(x, y)$ the variable bottom depth and H_0 the average depth (see Fig. 1).

The statistical mechanics theory is based on the assumption that a system obeying (1) tends toward an equilibrium state characterized by entropy maximization while maintaining the values of its constants of motion such as total energy.

$$E = \tfrac{1}{2} \int\!\!\int_S (\nabla\psi)^2 \, dxdy, \qquad (2)$$

and all the integrals of the powers of the absolute vorticity,

$$Q_n = \int\!\!\int_S q^n \, dxdy, \qquad (3)$$

where S is the basin area.

The calculation of the equilibrium states should ideally be performed by taking into account the infinite set of invariants (Eqs. 2–3). Calculations of this type are quite complex and have only been performed for specific cases with results which are often not easy to interpret practically (Miller, 1990; Robert and Sommeria, 1991; Weichman, 1993). An alternative and commonly used approach (Salmon *et al.*, 1976; Holloway, 1986) is to

consider only the linear and quadratic invariants, i.e., the total absolute vorticity Q_1, the total absolute enstrophy Q_2, and the total energy E. The equilibrium states one obtains in this way are an approximation of the real maximum entropy states valid for strong mixing cases. It can be shown that these approximated states are able to capture the main characteristics of the real states for a wide range of parameters (Chavanis and Sommeria, 1996), so that their use provide a simple and valid alternative to the use of the full equilibrium states.

The mean flow characteristic of the equilibrium states of (1) obtained using Q_1, Q_2 and E obeys the Fofonoff equation (Salmon *et al.*, 1976)

$$\langle q \rangle = \gamma \langle \psi \rangle + c \qquad (4)$$

where γ and c are constant Lagrangian multipliers which depend on the initial values of Q_1, Q_2 and E. In principle, the values of the parameters γ and c can be computed exactly given the values of the invariants Q_1, Q_2 and E, but the calculations can often be quite lengthy. In the following applications (as in most previous oceanographic applications, e.g., GS, WV) the parameters will be computed only approximately, using some simple arguments regarding the main characteristics of the flow.

Eq. (4) was first studied by Fofonoff (1954) for a closed basin with flat bottom, $q = \nabla^2 \psi + \beta y$, in a regime with realistically small values of energy, characterized by positive γ and boundary layer solutions. These solutions consist of two inertial gyres, an anticyclonic one in the northern part of the domain and a cyclonic one in the southern part. The gyres are characterized by a westward interior flow, $U_0 = -\beta/\gamma$, which recirculates along the boundaries in inertial boundary layers of thickness $\delta_I = \gamma^{-1/2}$. A rough *a priori* estimate of the size of the parameter γ, and therefore of the boundary layer thickness δ_I, as a function of the energy of the flow, can be given considering the global mass and energy budgets of the solution (GS, WV),

$$\delta_I = \gamma^{-1/2} \sim \epsilon^{2/3} L, \qquad (5)$$

where L is the basin dimension and ϵ is the Rossby number of the initial conditions defined as

$$\epsilon = U_{rms}/\beta L^2, \qquad (6)$$

with U_{rms} the root mean square velocity of the initial field.

The statistical mechanics prediction (4) has been investigated numerically. WV integrated directly the purely inertial quasi-geostrophic equation (1) and confirmed the emergence of equilibrium states with a mean flow satisfying relationship (4), in quantitative agreement with the theory. Other results by GS and C92 are also in qualitative agreement with (4), despite the fact that an eddy viscosity term F has been added to the right-hand side of (1) to represent the small scale processes:

$$\partial q/\partial t + J(\psi, q) = F.$$

These experiments show a tendency toward a Fofonoff state, even though the details of the final mean flows can sometimes deviate from (4). This will be discussed in more detail in Section 5.

The numerical experiments allow for a detailed study of the process of equilibration. They show that the equilibration has fundamental similarities with that observed in 2-D turbulence, in that it is produced by the basic process of a cascade of energy to large scales and of enstrophy to small scales. The 2-D and quasi-geostrophic cases, though, differ in some specific and important aspects that can be summarized as follows. In 2-D, the constraint of enstrophy conservation strongly inhibits the transfer of energy at small scales (e.g., Salmon, 1982b). In quasi-geostrophy, this constraint is partially relaxed because the conserved quantity is now the absolute enstrophy,

$$Q_2 = Z_2 - C \tag{7}$$

where $Z_n = \iint_s \zeta^n \, dx \, dy$ and $C = -2 \iint_s \zeta(\beta y + h^*)$. The conservation of (7) does not prevent the increase of Z_2 (and therefore the transfer of energy toward small scales), provided that the anticorrelation C between the relative vorticity and the generalized topography $(\beta y + h^*)$ increases commensurately. In quasi-geostrophy, then, some of the energy is allowed to move to small scales, leading to the emergence of boundary layers in the mean flow. During this process, Z_2 and C both increase, so that negative (positive) relative vorticity tends to migrate toward regions of high (low) absolute vorticity, developing a mean flow locked to the topography. For example, in the sloping boundary topography considered in the following experiments, the predicted mean flow locked to the topography is a cyclonic gyre.

It is worth noting that, when the hypothesis of no dissipation is relaxed, the enstrophy is expected to decay much more quickly than the energy during the evolution of the flow, since the enstrophy cascades toward smaller scales where the dissipation is more efficient. It can then be expected that for a weakly dissipative flow, the solution is characterized for intermediate times by a quasi-equilibrium state with approximately constant energy and with minimum enstrophy. This minimum enstrophy state can be explicitly calculated (e.g., Bretherton and Haidvogel, 1976), and results in the same Fofonoff state (4) predicted by statistical mechanics for purely inertial systems. Conceptually, the coincidence of maximum entropy and minimum enstrophy states is not surprising. The entropy maximization, in fact, can be considered as the underlying mechanism behind the nonlinear interactions, causing the process of enstrophy cascade, which in turn leads to the enstrophy minimization in presence of dissipation (e.g., Vallis and Maltrud, 1993).

b. Limitation of the theory outside quasi-geostrophy. The quasi-geostrophic equation holds in the limit of small nonlinearity (i.e., small Rossby number ϵ) and gentle topography (i.e., small fractional change of the depth, $\Delta H/H_0 \ll 1$). In this limit, the flow is close to geostrophy, so that the divergence is small and the velocity field is completely defined by the stream function ψ.

In the shallow water equations, the previous assumptions are relaxed and the flow can develop significant divergence. In the one-layer case considered here, this means that significant distortions of the free surface η are allowed (see Fig. 1). Consequently, the constants of motion of the system are also modified with respect to the quasi-geostrophic case. The total energy E has now a potential energy component in addition to the kinetic energy defined as

$$PE = \int_{-H}^{\eta} dz \int\int_S g\eta \, dxdy \qquad (8)$$

where η is the free surface elevation (Fig. 1). The other integral constants of motion take the form

$$PV_n = \int\int_S \Pi^n \, dxdy,$$

where Π is the potential vorticity defined as

$$\Pi = (\zeta + f)/h, \qquad (9)$$

with h being the total height of the fluid column $h = \eta + H$ (Fig. 1). In the quasi-geostrophic limit, the potential vorticity Π is related to the absolute vorticity q by $\Pi \cong q/H_0$.

The different structure of the invariants, and in particular of the total energy, which is no longer quadratic because of the potential energy component (8), makes the analytical calculation of the maximum entropy states more difficult in shallow water than in quasi-geostrophy. An example showing the difficulties of generalizing the statistical mechanics approach to shallow water is given by the work of Salmon (1982a).

In this paper, the behavior of inertial flows using the shallow water equations is investigated numerically. Flows with small Rossby number in a flat bottom basin are first considered. They are in the quasi-geostrophic range, but differ from flows studied in previous quasi-geostrophic experiments by the fact that the surface evolves freely (i.e., no rigid lid). A second set of experiments is presented for higher Rossby number and with steep topography, with an order one fractional change in the depth, placing them clearly outside the quasi-geostrophic approximation.

3. The numerical model

The shallow water numerical model used in this study is a single layer configuration of the primitive equation, isopycnic coordinate ocean model of Bleck and Boudra (1986). It consists of a momentum and a continuity equation:

$$\frac{d\mathbf{u}}{dt} + f\mathbf{k} \times \mathbf{u} = -g\nabla\eta + \mathbf{F}$$

$$\frac{\partial h}{\partial t} + \nabla(h\mathbf{u}) = 0 \qquad (10)$$

where g is the gravity, $\mathbf{u}$ is the horizontal velocity field and $\mathbf{F}$ is an eddy viscosity operator which simulates the action of small scale processes. Horizontal velocities and vorticity are defined as layer properties.

The operator $\mathbf{F}$ is expressed as

$$\mathbf{F} = A\nabla(h\nabla\mathbf{u})/h. \tag{11}$$

where A is the eddy viscosity coefficient. As shown by Gent (1993), the operator (11) has the important physical property of being energetically consistent, in the sense that it induces energy dissipation during the flow evolution. The operator $\mathbf{F}^* = A\nabla^2\mathbf{u}$, on the other hand, can actually generate energy in the context of the shallow water equations (10), as illustrated by Gent (1993). The operator $\mathbf{F}$, however, has the less desirable property of inducing in some cases an unphysical generation of enstrophy. The impact of the operator $\mathbf{F}$ on the solution was investigated by comparing the evolution in time of the enstrophy in cases with and without dissipation, with varying eddy viscosity and numerical resolution. The results indicate that, at least for the flows considered, the operator is correctly representing the process at work, namely consistently removing the enstrophy from the smallest resolved scales.

Tests were performed with either an energy conserving or potential enstrophy conserving (Sadourny, 1975) numerical formulation of the advective terms. No significant differences were observed, and all of the experiments presented in this paper were consequently performed with the potential enstrophy conserving scheme. This scheme was preferred since the conservation of potential enstrophy plays a key role in the set-up of the equilibrium solutions, as discussed in Section 2. For more details on the numerical model, the reader is referred to Bleck and Boudra (1986).

The numerical representation of the eddy viscosity operator as well as of the inertial terms requires additional boundary conditions with respect to the basic no normal flow conditions. As stated by Ierley (1990), there is no optimal choice for the boundary conditions. In this paper, all of the runs have been performed with the free-slip boundary condition (zero vorticity ζ on the boundary). Ideally, more detailed studies should be performed in the future to assess the impact of (a) different operators (biharmonic, deformation-dependent, . . .) and (b) different boundary conditions [no slip, super slip (Marshall, 1984)] on the equilibrium states.

4. General characteristics of the numerical experiments

Seven experiments (Table 1) are presented, in which the evolution of random initial conditions is studied in the absence of forcing. All of the experiments were performed on the β-plane in a square basin. They differ mainly in (a) the characteristics of the topography, (b) the values of the Rossby number ϵ of the initial conditions [Eq. (6)], (c) the values of the eddy viscosity coefficient A, and (d) the resolution.

The topography is flat in experiments E1, E1-ND, E2 and E2-ND, whereas it is given by steep sloping boundaries in ETOPO, ETOPO-HR and ETOPO-ND. In these experiments, the depth has a fractional change of order one, decaying linearly from $H = 4 \times 10^{-2}H_0$ at

Table 1. Table of the principal parameters for experiments E1, E2, ETOPO, ETOPO-HR. Experiments E1-ND, E2-ND and ETOPO-ND are identical to E1, E2 and ETOPO, respectively, except $\delta_D/\delta_I = 0$ (no dissipation). ϵ is the Rossby number (6) of the initial conditions, Z_1 is the total vorticity, $\|Z_1\|$ is the total vorticity norm, δ_D is the dissipative boundary layer computed as $(A/\beta)^{1/3}$ (with A the eddy viscosity), and δ_I is the inertial boundary layer computed from (5).

	E1	E2	ETOPO	ETOPO-HR
Topography	Flat bottom	Flat bottom	Sloping boundaries $(\Delta H/H_0 \sim 1)$	Sloping boundaries $(\Delta H/H_0 \sim 1)$
Initial ϵ	7.5×10^{-3}	2×10^{-3}	3.6×10^{-2}	3.6×10^{-2}
Initial $Z_1/\|Z_1\|$	-5×10^{-2}	-6×10^{-2}	4.5×10^{-2}	4.5×10^{-2}
δ_D/δ_I	3×10^{-2}	7.5×10^{-2}	5×10^{-2}	5×10^{-2}
Rossby radius	$.5L$	$.5L$	$1.1L$ (interior) $.22L$ (boundaries)	$1.1L$ (interior) $.22L$ (boundaries)
Integration time	$20\, T_{rms}$	$20\, T_{rms}$	$50\, T_{rms}$	$10\, T_{rms}$
Resolution	64×64	64×64	100×100	400×400

the boundaries to $H = H_0$ at a distance $L_s = 12 \times 10^{-2} L$ from the boundaries (Fig. 7a). The quasi-geostrophic assumption of gentle topography is not satisfied. The suffix ND means no dissipation and the suffix HR means high resolution.

The values of the Rossby numbers ϵ are on the order of 10^{-3} in the flat bottom experiments, and on the order of 10^{-2} in the cases with sloping boundaries (Table 1). The 10^{-3} values for ϵ are similar to those used in previous quasi-geostrophic experiments (GS, WV), while the 10^{-2} values are higher. The local Rossby numbers $\epsilon_0 = \zeta/f_0$ reach order 1 (or more) during the evolution of the flow inside the inertial boundary layers.

The values of the eddy viscosity A for E1, E2, ETOPO, ETOPO-HR are chosen sufficiently small so that the resulting loss of energy during the experiments is less than 10% of the initial value. The values of A can be characterized by the values of the viscous boundary layer thickness, estimated as $\delta_D = (A/\beta)^{1/3}$. In all of our experiments (Table 1), δ_D is approximately two orders of magnitude smaller than the inertial boundary layer δ_I [defined by (5)], indicating that the flow is clearly controlled by inertial processes. The experiments with suffix ND (E1-ND, E2-ND, ETOPO-ND), have no dissipation ($A = 0$), but are otherwise identical to the dissipative experiments. They have been introduced to allow a direct comparison with the theoretical results of statistical mechanics, which are obtained in the absence of dissipation. It is worthwhile to remark that the evolution of these experiments is expected to become increasingly more noisy as time progresses, since the enstrophy tends to accumulate at the smallest scales without being removed. The large-scale average flow, however, which is our primary interest here, is expected to maintain a smooth, physical behavior for much longer times. This is suggested both by the theory (e.g., Carnevale and Frederiksen, 1987), which predicts a stable mean flow pattern for inviscid truncated systems, and by previous quasi-geostrophic simulations (WV), which have shown the persistence of smooth average equilibrium solutions for times longer than those considered in the present experiments.

The resolution is 64×64 horizontal grid points for the E1 and E2 experiments, $100 \times$
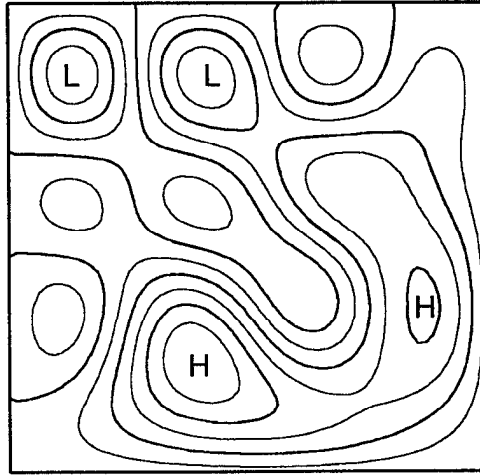
Figure 2. Initial free surface field for E1.

100 for the ETOPO experiments, and 400 × 400 for ETOPO-HR (Table 1). Since the focus of this paper is the study of the dynamics controlled by inertial processes, resolution of the inertial boundary layer δ_I is a fundamental requirement for the simulations. The above values for the number of grid points ensure that δ_I is resolved in all the experiments (although only marginally in the E2 experiments, by one grid point). The viscous boundary layer δ_D, on the other hand, is smaller than δ_I by almost two orders of magnitude and is therefore not expected to play a fundamental role in the large-scale structure of the solution. This point is discussed in detail in Section 6b, regarding the high resolution experiment ETOPO-HR in which δ_D is resolved. The comparison between ETOPO-HR and ETOPO, identical except for the resolution, indicates that indeed the viscous boundary layer does not affect the large-scale average flow.

The duration of the experiments is determined using the intrinsic scale of nonlinearity, $T_{rms} = L/U_{rms}$, which represents the typical time of advection through the basin. The E1 and E2 experiments were integrated for 20 T_{rms}, the ETOPO experiments for 50 T_{rms}, and ETOPO-HR, which requires a substantially longer time of integration because of the high resolution, for only 10 T_{rms} (Table 1). The time step for the integration is very small in order to resolve the fast propagating surface gravity waves. Finally, all results are presented in nondimensional form.

5. Experiments with flat bottom

The four experiments E1, E1-ND, E2-ND and E2-ND were configured with a flat bottom (Table 1). The initial conditions are a collection of random eddies in geostrophic balance, with the energy confined to wavenumbers 3 and 4. The structure of the eddies is the same for all the experiments and is shown in Figure 2. The energy levels are different with corresponding values of $\epsilon = 7.5 \times 10^{-3}$ for E1 and E1-ND and $\epsilon = 2 \times 10^{-3}$ for E2 and

E2-ND (Table 1). These values are of the same order of magnitude as those considered by other authors for quasi-geostrophic experiments (GS, WV, C92). However, the experiments described in this paper possess a free evolving surface, implying that differences may exist from the quasi-geostrophic experiments that used the rigid lid approximation. The chosen basin parameters, in fact, are such that the Rossby radius of deformation, $a = (gH_0)^{1/2}/f_0$, is $a = \frac{1}{2}L$, so that the rigid lid approximation does not hold.

The initial evolution of the experiments (E1, E1-ND, E2 and E2-ND) is similar to the corresponding quasi-geostrophic experiments. During the first 1–2 T_{rms}, a piling up of energy and enstrophy occurs at the western boundary, due to the propagation and reflection of Rossby waves. In the following T_{rms} periods, the energy is advected along the boundaries, setting up the inertial boundary layers. This leads to the inertial segregation of vorticity, with the negative (positive) vorticity forming an anticyclonic (cyclonic) gyre in the northern (southern) part of the basin. During this evolution, the enstrophy Z_2 increases. At times longer than 5 T_{rms}, when the two gyres have already formed, the enstrophy starts to oscillate, decreasing slowly on the average in E1 and E2 because of the dissipation. This is an indication that the system is approaching its equilibrium state. The structure of the two inertial gyres depends on the value of ϵ.

For both series of experiments, the numerical integration has been carried out for 20 T_{rms}. During the last 5 T_{rms} computations of the average potential vorticity Π and of the free surface height η have been performed. Compared to the quasi-geostrophic experiments (GS, C92, WV), the total time and the average time of our experiments are considerably shorter because the numerical integration is much more demanding (small integration time step). This also means that our averages are slightly noisier than those of the corresponding quasi-geostrophic experiments. A comparison between the 5 T_{rms} averages and the averages computed over the last 3 T_{rms}, however, shows very little differences in the fields and suggests that the results are representative of the equilibrium.

a. Equilibrium states for high Rossby number. In the high Rossby number experiment E1, the two gyres are well defined in the instantaneous fields (Fig. 3a) and they vary in a manner similar to normal mode oscillations. The time-average of the free surface η for E1 is presented in Figure 3b. The similarity between the E1 results and the "Fofonoff gyres" obtained in analogous quasi-geostrophic solutions (GS, C92, WV) is evident. Notice that the asymmetry between the northern and southern gyre is due to the initial conditions, which possess a net negative vorticity (see Table 1). The results for E1-ND (not shown) are similar to the E1 results for the time-average $\langle \eta \rangle$ field, whereas the average Π field differs more, with noisier fields in E1-ND due to the lack of dissipation. Also, as expected, the instaneous fields of η and Π display more noise in the E1-ND experiment.

Quantitative tests of the resemblance of the numerical solutions to the Fofonoff solutions (4) are routinely done in the quasi-geostrophic context (GS, C92, WV, CH) by creating scatter diagrams of the time-averaged $\langle \psi \rangle$ and $\langle q \rangle$ and verifying whether their relationship is linear. For our experiments, in the shallow water context, we have created the scatter
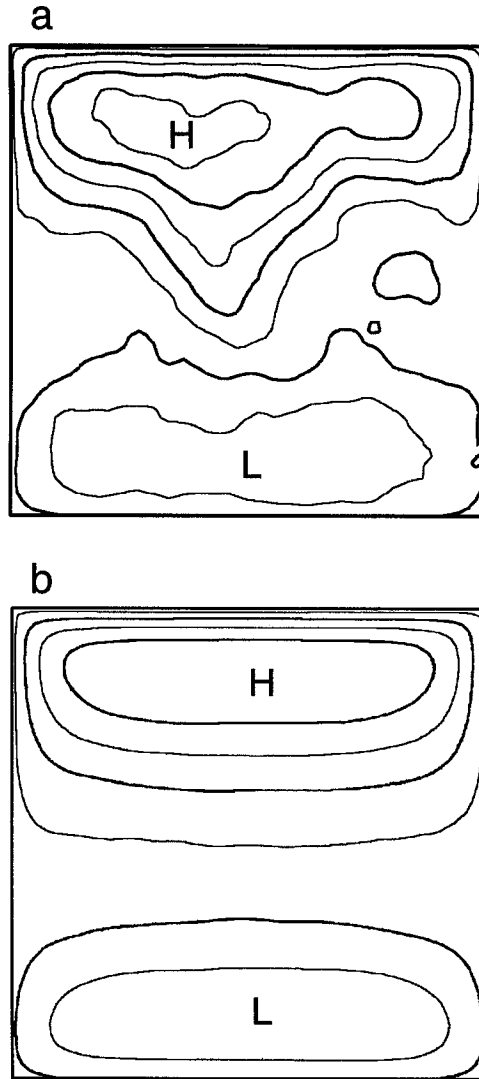
a

b

Figure 3. (a) Instantaneous free surface field for E1 at $t = 10\ T_{rms}$; (b) Time average free surface field for E1 computed over the time interval 15–20 T_{rms}.

diagrams of the average of the quantities

$$\psi^* = \eta g/f_0$$
$$q^* = \Pi H_0$$

(12)

which reduce to ψ and q in the quasi-geostrophic limit. This difference may lead to some deviations from the quasi-geostrophic results.
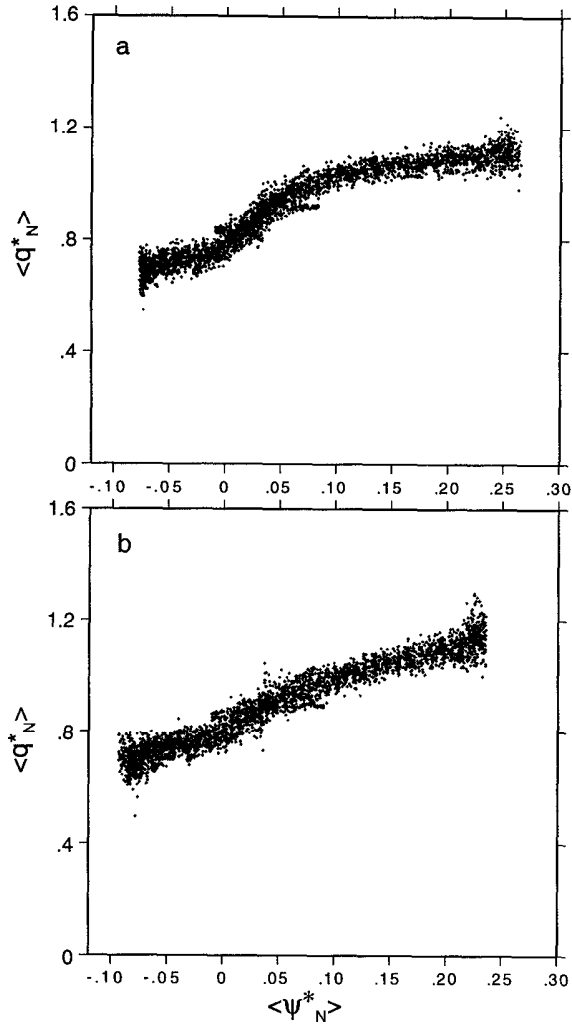
Figure 4. Scatter plots of the nondimensionalized $\langle \psi_N^* \rangle$ versus $\langle q_N^* \rangle$ with the boundary points removed, $\psi_N^* = \psi^*/U_{rms}L$, $q_N^* = q^*/f_0$. (a) E1; (b) E1-ND.

The scatter diagrams for E1 and E1-ND are displayed in Figure 4a,b, respectively. As expected, the results are noisy, but the general trend is clear. The E1-ND results (Fig. 4b), obtained with no dissipation, show an almost linear relationship between $\langle \psi^* \rangle$ and $\langle q^* \rangle$, whereas for E1 (Fig. 4a), with dissipation, there is a flattening in the regions corresponding to the gyre interiors, indicating a homogenization of $\langle q^* \rangle$. These results are very similar to results obtained with the quasi-geostrophic equation in the same range of ϵ (e.g., GS). In particular, a similar deviation from linearity and an increase in the extent of the flattened regions was observed by C92 and WV for a higher dissipation.
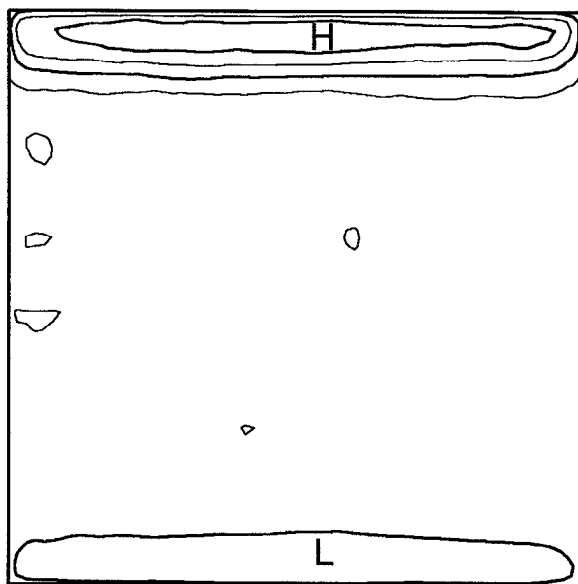
Figure 5. Time average free surface field for E2 computed over the time interval 15–20 T_{rms}.

From the scatter diagram of E1-ND (Fig. 4b), the parameter γ of proportionality between $\langle\psi^*\rangle$ and $\langle q^*\rangle$ can be estimated together with the space scale $\delta_I = \gamma^{-1/2}$, characteristic of the inertial boundary layer. Linearly fitting the data shown in Figure 4b gives a value of $\delta_I \sim 6 \times 10^{-2}L$. When compared to the *a priori* estimate (5), $\delta_I \sim \epsilon^{2/3}L \sim 4 \times 10^{-2}L$, this value is of the same order of magnitude, although slightly smaller. These values are in good qualitative agreement with the boundary layer thickness shown by the average $\langle\eta\rangle$ field in Figure 3b.

b. Equilibrium states for low Rossby number. The Rossby number is smaller in E2 and E2-ND than in E1 and E1-ND. The inertial gyres are not as well defined in the instantaneous fields as in the high Rossby number experiments. They are, however, present in the average fields, computed over the same period as for the E1 experiments. Their shapes differ from those of E1 and E1-ND since the gyres do not cover the whole basin but are confined to regions near the northern and southern boundaries, as illustrated in Figure 5 for E2. The results for E2-ND (not shown) are similar but slightly noisier. As in E1, the north-south asymmetry is due to the net negative vorticity in the initial conditions (Table 1).

The fact that the gyres are close to the boundaries in E2 produces scatter diagrams of $\langle\psi^*\rangle$ versus $\langle q^*\rangle$ that are different from those for E1 and E1-ND. As is apparent from Figure 6a,b (computed for E2 and E2-ND, respectively), the regions of the two gyres are characterized by two different and almost linear functional relationships, separated by a region of mean
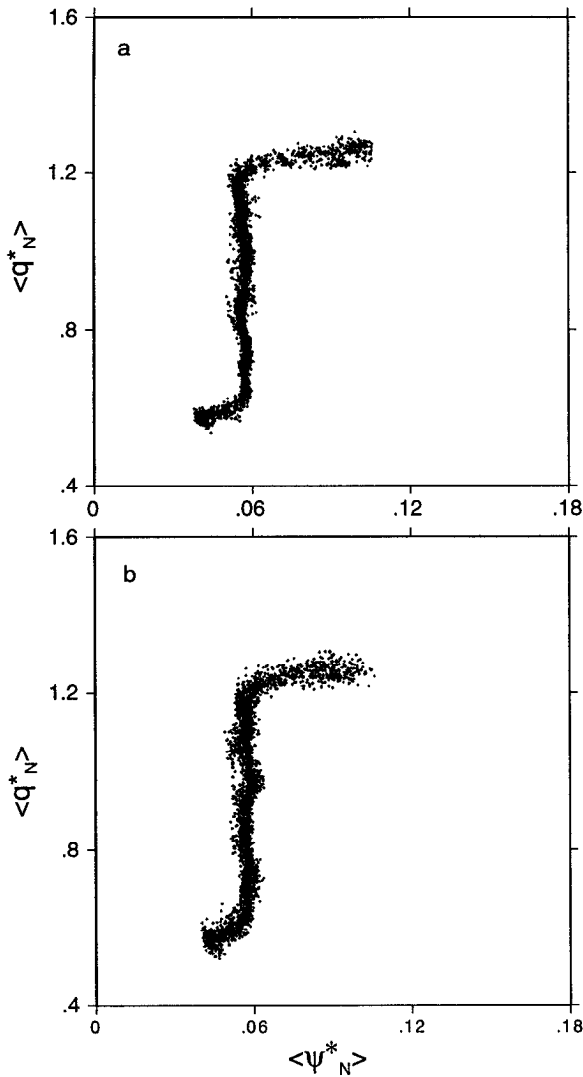
Figure 6. Scatter plots of the nondimensionalized $\langle \psi_N^* \rangle$ versus $\langle q_N^* \rangle$ with the boundary points removed, $\psi_N^* = \psi^*/U_{rms}L$, $q_N^* = q^*/f_0$. (a) E2; (b) E2-ND.

flow close to zero. Dissipation tends to flatten the straight lines inside the gyres as was the case for E1-ND.

Even though the linear relationship is not valid everywhere in the solution, the scale parameter δ_I can still be evaluated locally from the E2-ND scatter diagram (Fig. 6b). The well-defined slope in the region of the main anticyclonic gyre was considered and gave a value for δ_I of $2 \times 10^{-2}L$. The *a priori* estimate (5) gives a value $\delta_I \sim 1.6 \times 10^{-2}L$, which

is as in the E1-ND case slightly lower. As in E1-ND, the estimates of δ_I are in agreement with the boundary layer thickness shown in Figure 5.

Similar patterns for the average gyres and for the scatter diagrams have been obtained for comparable values of ϵ in the quasi-geostrophic experiments (GS, CW, C92). When the Rossby number decreases, all of the quasi-geostrophic viscous experiments, regardless of the specific form of the eddy viscosity operator and of the boundary conditions, show a tendency for the gyres to contract with a scatter diagram shape very similar to those presented in Figure 6. This is not the case for purely inertial runs, as pointed out by WV, where the Fofonoff equilibrium state is reached for any value of the Rossby number ϵ, with a well defined linear relationship between $\langle \psi^* \rangle$ and $\langle q^* \rangle$ over the whole basin. It is the introduction of boundary conditions (free slip, no slip, super slip . . .), needed for the inertial terms and for the eddy viscosity operator, which induces the deviation from the Fofonoff state. In particular, C92 and WV suggest that the boundary conditions tend to control the shape of the solutions more than the eddy viscosity operator. This is supported by the fact that experiment E2-ND, with zero dissipation and free slip boundary conditions, gives results similar to those of the dissipative experiments having the same boundary conditions.

One possible explanation for the gyre contraction mechanism is that any boundary condition added to the basic condition of no normal flow will inhibit to some degree the free advection of vorticity around the boundary, thereby modifying the nature of the inertial boundary currents close to the walls. The inertial currents in the presence of the boundary conditions are then likely to have different stability properties with respect to the purely inertial currents, and it is possible that, for certain parameter ranges, the reduced stability does not allow the establishment of inertial gyres over the whole basin.

In summary, the results presented in this section illustrate the fact that the numerical integration of the shallow water equations with a free surface and of the quasi-geostrophic equations with a rigid lid behave in a similar fashion. This indicates that the role of the free surface can be considered negligible, at least for a quasi-geostrophic regime. These results also illustrate a similar sensitivity of the two numerical models to the boundary conditions. The tendency toward the Fofonoff equilibrium flow is verified, but, as in quasi-geostrophy, the introduction of dissipation and of additional boundary conditions modifies the final solutions, especially for low Rossby numbers.

6. Experiments with sloping boundaries

Three experiments, ETOPO, ETOPO-ND (with and without eddy viscosity respectively), and ETOPO-HR (with higher resolution), were performed with sloping boundaries (Table 1). The slope is steep (equal to 2×10^{-2}), with the depth varying linearly from $4 \times 10^{-2} H_0$ at the boundaries to H_0 at the end of the sloping region of size $L_s = 12 \times 10^{-2} L$ (Fig. 7a). The value of the Rossby radius of deformation a is greater than the basin size in the flat bottom interior, $a = 1.12 \times L$, and it decreases on the slope reaching a minimum
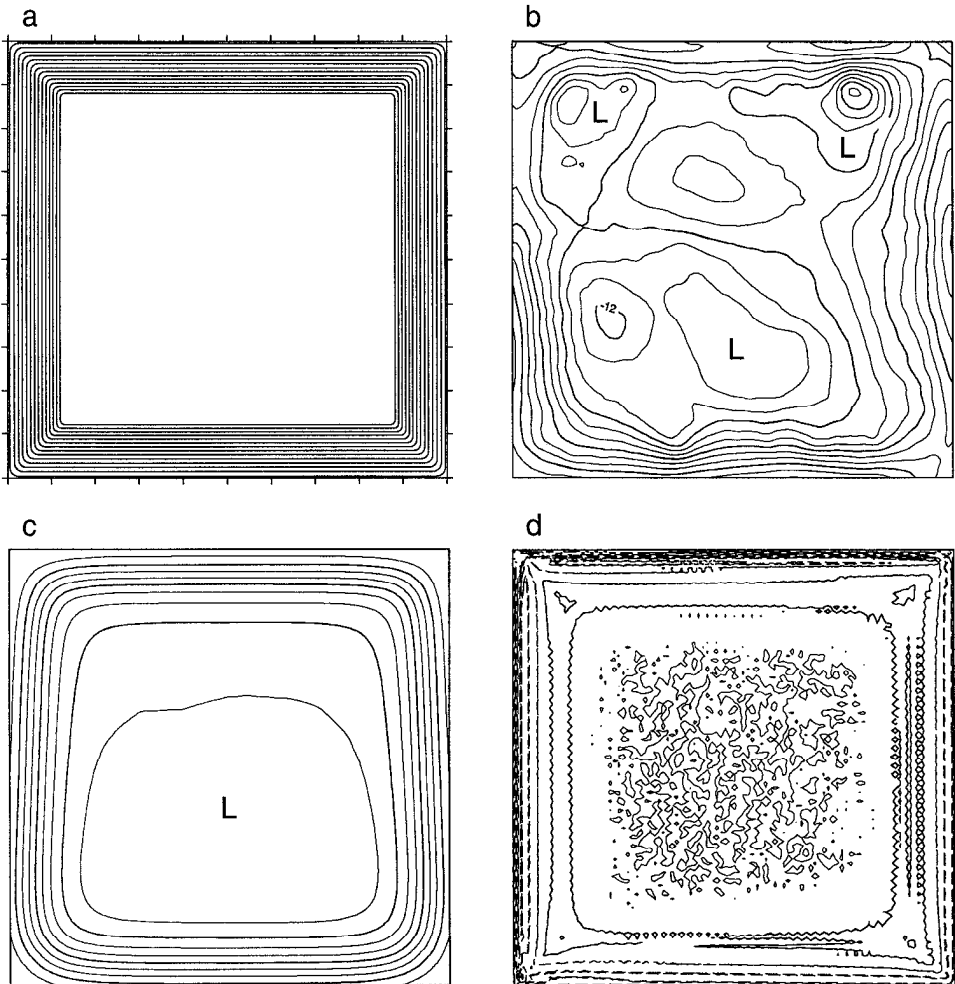
Figure 7. (a) Topography for ETOPO experiments; (b) Instantaneous free surface field for ETOPO at $t = 4T_{rms}$; (c) Time average free surface field for ETOPO computed over the time interval 40–50 T_{rms}; (d) time average vorticity for ETOPO computed over the time interval 40–50 T_{rms}. The dashed lines indicate negative values of vorticity.

value $a = .22 \times L$ at the boundaries. Note that this value, even though smaller than the basin width, is greater than the width of the slope region L_s. The initial conditions have a similar structure to those for the flat bottom experiments, except that now the net vorticity Z_1 is positive (Table 1). The reason for this choice is that the equilibrium flow is expected to be cyclonic and its set-up is then facilitated by the presence of a positive Z_1. The energy of the initial conditions is higher than in the previous experiments, corresponding to a Rossby number $\epsilon = 3.6 \times 10^{-2}$ (and local Rossby numbers ϵ_0 of order 1), which, when combined with an order 1 change in bottom topography, clearly places this experiment outside the

quasi-geostrophic range. The quasi-geostrophic experiments of WV and CH, on the other hand, were less energetic with topography not as steep, and were performed on an f-plane. In the following Section 6a, we discuss first the two lower resolution experiments, ETOPO and ETOPO-ND, which have been run for a longer integration time. The effects of resolution will then be discussed using the results of ETOPO-NR (Section 6b).

a. The low resolution experiments. The initial evolutions of ETOPO and ETOPO-ND are very similar, but they differ significantly from the evolution of the flat bottom experiments. During the first few T_{rms}, in fact, the flow does not show a western intensification, but rather is dominated by long topographic waves propagating along the slope. The long wave activity determines an increase in the total potential energy PE, which approximately doubles in value during this first phase. We remark that, despite this increase, PE is always more than one order of magnitude smaller than the total kinetic energy, as is expected considering the size of the Rossby radius. Also, the waves appear to have a strong gravity component, as suggested by the ageostrophic effects present in the solution. At about 4 T_{rms}, a rectified cyclonic current starts to emerge along the slope, detectable also in the instantaneous fields (see Fig. 7b for ETOPO). During this set-up, the enstrophy Z_2 continues to increase until about 7 T_{rms}, when Z_2 begins to oscillate suggesting that an equilibrium state is being approached. At this point, the cyclonic gyre is well defined in the instantaneous fields and shows normal mode oscillations. One interesting point is that the cyclonic gyre has a velocity maximum located at a distance $\sim 1/3 L_s$ from the boundary. The presence of this maximum generates a boundary layer of negative vorticity around the cyclonic gyre, which, as noted by CH, can be explained in terms of total vorticity conservation. The negative vorticity layer, in fact, counterbalances the positive vorticity of the remainder of the cyclonic circulation, so that the total vorticity value in the basin remains positive but small, as in the initial conditions. This mechanism can be contrasted with the one at work in the flat bottom gyres (experiments E1, E2), where the vorticity balance is maintained through the formation of the two separate gyres (one anticyclonic and one cyclonic) and the velocity maximum occurs at the boundaries.

The initial evolution of the quasi-geostrophic experiments of WV and CH is quite different from the evolution of our experiments. In their simulations, the approach to the equilibrium state is much slower and is characterized by an intermediate state in which, in addition to the cyclonic gyre present along the boundaries, a counter-rotating anticyclonic gyre is present in the center of the basin. This anticyclonic gyre, not present in our experiments, slowly decays in WV and CH, so that the equilibrium state becomes characterized by the cyclonic gyre only. The equilibration time is greater than 100 T_{rms}.

The observed differences between our primitive equation experiments and the quasi-geostrophic experiments are due to a combination of factors. First of all, the primitive equation solutions have an additional mechanism of energy transfer, given by the gravity waves, which, as seen above, play a role in the set-up. In addition to this, the CH and WV solutions are performed on an f-plane (in contrast to our β plane solutions). In CH and WV,

all the contours of f/H are closed and the Rossby waves are completely trapped by the topography. In our case, instead, the β-effect, even if weak with respect to the topographic effect, does induce an opening of the contours at the boundaries, especially in the northern part of the basin, facilitating the generation of small-scale energy by wave reflection and its reorganization in inertial boundary currents. Finally, the quasi-geostrophic experiments of CH and WV are obtained with zero total vorticity (in contrast to our positive vorticity initial conditions). The zero vorticity condition may be responsible for a more complex adjustment, since the negative vorticity boundary layer must be stronger in order to cancel completely the positive vorticity of the rest of the cyclonic circulation.

ETOPO and ETOPO-ND have been integrated for 50 T_{rms}. The average η of ETOPO, computed over the last 10 T_{rms}, is shown in Figure 7c. A similar result was obtained for ETOPO-ND and is therefore not illustrated. The cyclonic gyre is clearly evident, with an intensification in the southern part of the domain. The isolines of η also indicate the presence of the velocity maximum on the slope. This is illustrated by the time average ζ diagram (Fig. 7d), which shows a layer of negative vorticity close to the boundaries. Qualitatively, the structure of the mean flow appears compatible with the expected Fofonoff solution (4) in the presence of sloping boundaries and on a β-plane. The Fofonoff solution with sloping boundaries alone and without the β-plane is a symmetric cyclonic gyre, as studied by CH and WV. The β-effect, on the other hand, as illustrated by the flat bottom experiments, tends to generate an anticyclonic circulation at the northern boundary and a cyclonic one at the southern boundary. Its influence on the cyclonic gyre is therefore to weaken the northern part and to strengthen the southern part of the gyre.

The resemblance to the Fofonoff solution is tested quantitatively as in the previous sections by computing the scatter diagram of $\langle\psi^*\rangle$ versus $\langle q^*\rangle$. The results for ETOPO are shown in Figure 8. The results for ETOPO-ND are not shown as no significant difference is observed between the two. The general trend is an almost linear relationship in the interior region, away from the boundaries, which corresponds to the positive and high values of $\langle\psi^*\rangle$. In the region very close to the boundaries, though, there are deviations from the Fofonoff flow as indicated by the more complex and multivalued relationship between $\langle\psi^*\rangle$ and $\langle q^*\rangle$. The lines of approximately constant $\langle q^*\rangle$ at the extreme values ($\langle q^*\rangle \sim 4$, $\langle q^*\rangle \sim -1$ in Fig. 8) correspond to the grid points in the rows closest to the walls. The other lines of approximately constant $\langle q^*\rangle$, which can be noticed in the region where $\psi^* > 0$, correspond to points along isobaths characterized by increasing and discretized depth. The changes in ψ^* along each line reflect the changes of the free surface along the isobaths, suggesting the occurrence of ageostrophic processes. A closer inspection of the average η field (Fig. 7c) shows that indeed the surface height η is not constant along the boundaries and decreases away from the corners, accelerating and decelerating the flow according to Bernoulli's theorem.

As for the flat bottom experiments (E1, E2), we can use the $\langle\psi^*\rangle$ versus $\langle q^*\rangle$ scatter diagram (Fig 8) to estimate the constant of proportionality γ between $\langle\psi^*\rangle$ and $\langle q^*\rangle$ (4) and the space scale $\delta_I = \gamma^{-1/2}$ associated with it. The *a priori* estimate (5) for δ_I, however,
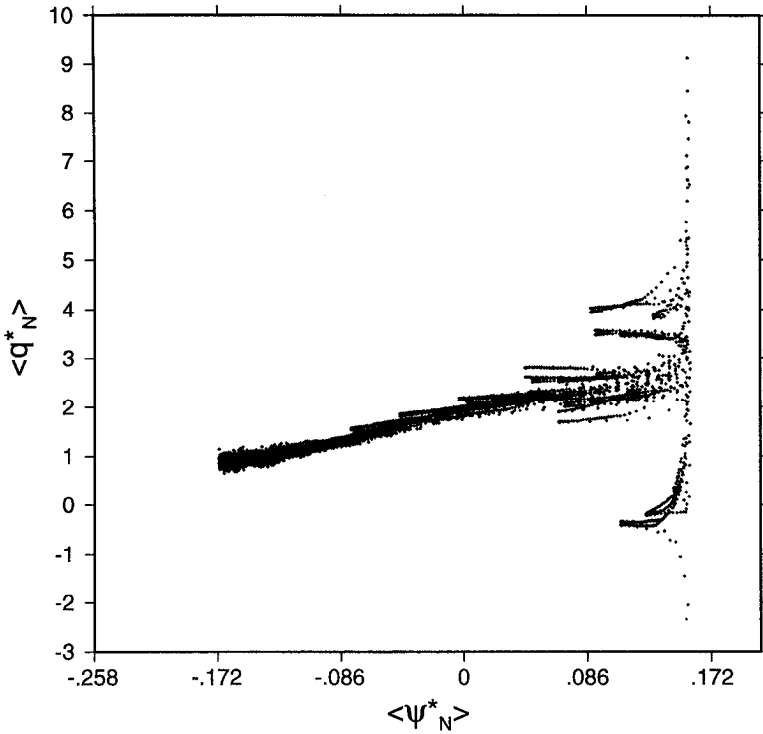
Figure 8. Scatter plot of the nondimensionalized $\langle \psi_N^* \rangle$ versus $\langle q_N^* \rangle$ with the boundary points removed, $\psi_N^* = \psi^*/U_{rms}L$, $q_N^* = q^*/f_0$, for ETOPO.

which was used for the E1, E2 experiments, does not apply in the case of sloping boundaries since it is based on the flat bottom solution. In the following we suggest a modification of the estimate (5), valid for the sloping boundary solution. The scale δ_I represents the thickness of the boundary layer in (4), i.e., the scale where the relative vorticity term $\zeta = \nabla^2 \psi$ in (4) is not negligible. Outside this boundary layer, at scales larger than δ_I, the interior flow obeys

$$f + h^* \sim \gamma \langle \psi_0 \rangle + c. \tag{13}$$

In the case of flat bottom, the interior flow computed from (13) is westward, $U_0 \sim -\beta(\delta_I)^2$, and it recirculates along the boundaries in the boundary layers. In the case of sloping boundaries, instead, if the boundary layer is sufficiently small with respect to the slope region, $\delta_I < L_s$, the interior flow is dominated by the cyclonic circulation induced by the slopes. Its magnitude can be computed easily from (13) (using the fact that the β-effect on the slope can be neglected since it is at least one order of magnitude smaller than the topography effect), and is given by $|U_0| \sim f_0 \Delta H \delta_I^2/L_s H_0$. Inside the boundary layer, this velocity varies and decreases toward the boundaries to form a negative vorticity layer. A very rough estimate of δ_I can be obtained using vorticity and energy conservation by

assuming that the energy in the boundary layer is negligible with respect to the interior energy on the slope,

$$\delta_I \sim \left(\frac{U_{\text{rms}}}{f_0 L} \frac{H_0}{\Delta H}\right)^{1/2} \left(\frac{L_s}{2L}\right)^{1/4} L. \tag{14}$$

The estimate of δ_I from the scatter diagram (Fig. 8), neglecting the points next to the boundaries, gives $\delta_I \sim 5 \times 10^{-2}L$. This value is in agreement with the simple estimate (14), which gives $\delta_I \sim 5.8 \times 10^{-2}L$, and with the boundary layer thickness suggested by the $\langle \zeta \rangle$ field (Fig. 7d).

b. The high resolution experiment. The effects of resolution have been studied comparing the results of ETOPO with those of ETOPO-HR. The two experiments have the same parameters except for the resolution, which is four times greater (400 × 400) in ETOPO-HR (Table 1). The principal points we address in this comparison are the effects of (a) better resolution of the topographic slope, and (b) resolution of the viscous boundary layers. The viscous boundary layer is resolved by one point in ETOPO-HR (a marginal resolution comparable to that of the quasi-geostrophic experiments of WV and CH), while it is not resolved in the other experiments presented in the previous Section 6a. In Section 4, the lack of resolution of the viscous boundary layer was justified by arguing that the dynamics are mostly controlled by inertial processes, so that the details of the viscous boundary layer are not likely to influence the large-scale structure of the flow. Here this assumption is tested and quantified. Because of the high resolution, the ETOPO-HR experiment is computationally much more demanding than the other experiments, and its integration has been limited to the first 10 T_{rms}. However, as will be shown, this is sufficient time to draw significant conclusions.

The initial evolution of ETOPO-HR is similar to the evolution of ETOPO and is dominated by wave activity on the slope, leading to a rectified cyclonic current. Some quantitative differences are present, however, between the two solutions. First, despite the same eddy viscosity coefficient A in the two experiments, ETOPO-HR is noticeably smoother than ETOPO, as can be seen in the instantaneous η fields at $t \sim 4\ T_{\text{rms}}$ (Fig. 7b, 9a). This is due to the fact that the dissipation acts mainly at the cutoff wavenumber, where enstrophy tends to accumulate under the action of the nonlinear cascade. Since higher wavenumbers are available in ETOPO-HR than in ETOPO, the scale selective dissipation (11) acts more efficiently in removing the noise from the small scales. An other difference between the solutions is that ETOPO-HR tends to have higher PE than ETOPO initially. This is consistent with a more pronounced distortion of the free surface on the slope and wave activities in ETOPO-HR (Fig. 7b–9a). Since the wavenumber space in ETOPO-HR is considerably larger than in ETOPO (16 times), the cascade process occurs differently in the two experiments. In ETOPO-HR, more energy is available to move toward large scales, since the enstrophy cascade can proceed at higher wavenumbers and can be trapped initially in topographic waves. Different resolution in the two experiments also implies
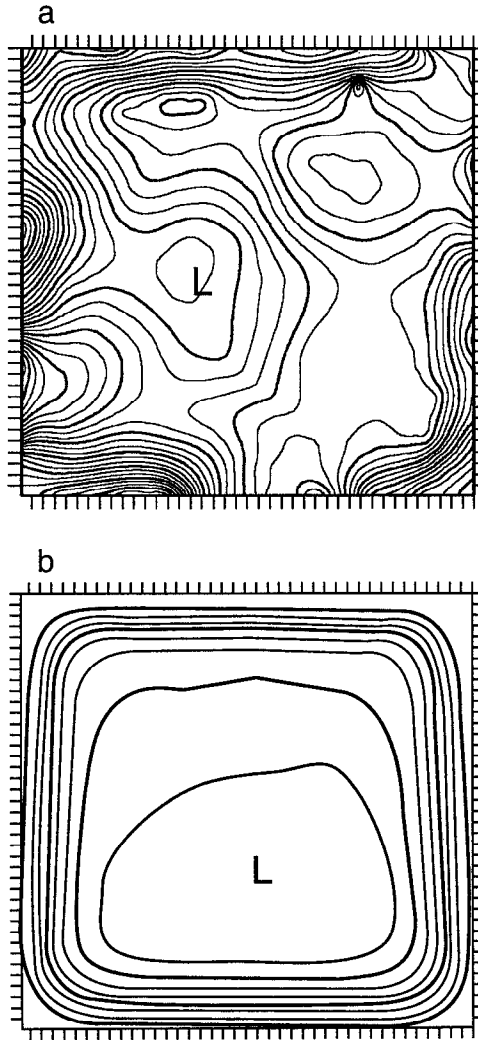
a

b

Figure 9. (a) Instantaneous free surface field for ETOPO-HR at $t = 4\ T_{rms}$; (b) Time average free surface field for ETOPO-HR computed over the time interval 7–10 T_{rms}.

different discretization of the topography. In the lower resolution experiment ETOPO, the depth change between grid points on the slope is four times bigger than in ETOPO-HR. This may imply that a cross-topography flow is more inhibited in ETOPO, as such a flow would require an abrupt change in either relative vorticity or free surface elevation.

Like ETOPO, ETOPO-HR appears to converge toward the equilibrium state after approximately 7 T_{rms}. The average $\langle \eta \rangle$ computed over the last 3 T_{rms} of the experiment (between 7 and 10 T_{rms}) is shown in Figure 9b. This average is not expected to be completely representative of the final equilibrium mean flow, since it is performed too early

in the evolution and for a short time. Nonetheless, it does capture most of the equilibrium characteristics, as can be seen by comparing Figure 9b to Figure 7c, which shows the average $\langle \eta \rangle$ for ETOPO computed between 40 and 50 T_{rms}. In both averages, the cyclonic gyre is very clear, with similar structure even close to the boundaries. The only quantitative difference is a higher surface displacement in ETOPO by approximately 10%. In order to verify whether or not this is simply an effect of the early averaging for ETOPO-HR, an average over the same interval (between 7 and 10 T_{rms}) was performed for ETOPO. The average $\langle \eta \rangle$ (not shown) shows the same surface displacement as in ETOPO-HR, confirming that the equilibrium state is not yet completely achieved. The averages $\langle \zeta \rangle$ and the $\langle \psi^* \rangle$ versus $\langle q^* \rangle$ scatter diagram for ETOPO-HR have also been computed. Comparisons with the ETOPO results also show good quantitative agreement. We therefore conclude that the viscous boundary layer does not appear to affect the characteristics of the large-scale equilibrium flow.

In summary, the results presented in this section indicate that the tendency toward the Fofonoff flow persists also for flows outside of the quasi-geostrophic range. Ageostrophic effects tend to modify the details of the flow, especially close to the boundary, but the main characteristics of the mean flow are still well described by the quasi-geostrophic equilibrium state.

7. Summary and concluding remarks

In this paper, the properties of the inertial gyre solutions of a one-layer primitive equation ocean model (Bleck and Boudra, 1986) have been investigated in detail. The main purpose was to verify whether or not the inertial solutions obtained with primitive equations can be described using the statistical mechanics results developed in the framework of quasi-geostrophic theory. The experiments were "initial release" experiments, in the limit of very small or zero dissipation, with varying Rossby numbers and varying topography. The process of equilibration of the solutions was studied in detail, and the final states were compared with the Fofonoff solutions predicted by the statistical mechanics theory.

In a first series of experiments performed with flat bottom and with Rossby numbers in the quasi-geostrophic range, the rigid lid condition was not imposed and the surface gravity waves were included explicitly. The experiment results were then compared to results obtained with the quasi-geostrophic equation with rigid lid (GS, C92, WC). Both the equilibration process and the characteristics of the equilibrium states turned out to be very similar to the quasi-geostrophic rigid lid experiments, suggesting that the free surface contribution is negligible, and that the quasi-geostrophic and primitive equation models behave in a similar fashion.

For the experiments with high Rossby number and with no dissipation, the equilibrium average solutions are given by two inertial gyres which extend over the whole basin and which are well characterized by the Fofonoff linear relationship between the stream

function $\langle \psi^* \rangle$ and the potential vorticity $\langle q^* \rangle$. The slope of the $\langle q^* \rangle$ versus $\langle \psi^* \rangle$ relationship has been computed and found to be in agreement with *a priori* estimates based on the equilibrium statistical mechanics prediction. In the presence of dissipation, q^* tends to homogenize inside the gyres, resulting in a flattening of the $\langle \psi^* \rangle$ to $\langle q^* \rangle$ relationship. In the case of a low Rossby number, the gyres do not cover the whole basin and are confined to near the northern and southern boundaries. The scatter diagram of $\langle \psi^* \rangle$ versus $\langle q^* \rangle$ shows two separated regions with a linear relationship, corresponding to the two-gyre regions. This phenomenon of gyre contracton, which is present also in the quasi-geostrophic experiments, is not yet completely understood and should be addressed in future work. A reasonable hypothesis is that it depends on the stability properties of the inertial boundary currents, as a function of the Rossby number and of the nature of the boundary conditions.

A second series of experiments was performed outside the quasi-geostrophic range for sloping boundaries with order one fractional depth change and higher Rossby number. The equilibration process is different from that in the case with flat bottom, and it appears to be dominated by topographic waves propagating on the slope and leading to a rectified cyclonic flow. The results were compared to quasi-geostrophic results obtained with a similar but less steep topography, lower Rossby number, and on an f-plane (WV, CH). The process of equilibration is different in these quasi-geostrophic flows, probably because of the absence of topographic gravity waves, and also because of the different nature of the topographic Rossby waves in the absence of β. The characteristics of the equilibrium states are, however, similar in the quasi-geostrophic and primitive equation experiments, with an average flow given by a cyclonic gyre extending over the whole basin. The $\langle q^* \rangle$ versus $\langle \psi^* \rangle$ scatter diagram shows an almost linear relationship, at least away from the boundaries. Close to the boundaries, the presence of ageostrophic effects modifies the flow, but the overall structure appears well described by the Fofonoff flow. As for the flat bottom case, the slope of the $\langle q^* \rangle$ versus $\langle \psi^* \rangle$ relationship has been computed and compared to an *a priori* estimate.

In the framework of the topographic experiments, we have also performed an investigation on the effects of resolution. The results indicate that, in weakly dissipative flows, the lack of resolution of the viscous boundary layers does not affect the structure of the equilibrium mean flow. On the other hand, some aspects of the process of equilibration appear to be affected by the resolution, probably because of the changes in the topography discretization and because of the changes in the process of nonlinear cascade. Further investigations on the exact mechanisms through which the equilibration occurs and on its dependence on the resolution are planned for the future.

In conclusion, the experiments presented in this paper suggest that, despite the fact that the theory was developed for quasi-geostrophic motions, equilibrium statistical mechanics theory is able to capture the main aspects of the inertial equilibrium states which are outside the range of validity of quasi-geostrophy. The results also support the hypothesis of Holloway (1992) and encourage the development of subgrid scale parameterizations for

OGCMs based on the statistical mechanics predictions (Eby and Holloway, 1994). An investigation of the effects of forcing and dissipation, and of the practical implementation of these parameterizations, is presently underway (Roubicek *et al.,* 1995).

REFERENCES

Alvarez, A., J. Tintore, G. Holloway, M. Eby and J. M. Beckers. 1994. Effect of topographic stress on the circulation in the Western Mediterranean. J. Geophys. Res., *99,* 16053–16064.

Bleck, R. and D. B. Boudra. 1986. Wind-driven spin up in eddy-resolving ocean models formulated in isopycnic and isobaric coordinates. J. Geophys. Res., *91,* 7611–7621.

Bretherton, F. P. and D. B. Haidvogel. 1976. Two dimensional turbulence over topography. J. Fluid Mech., *78,* 129–154.

Carnevale, G. F. and J. D. Frederiksen. 1987. Nonlinear stability and statistical mechanics of flow over topography. J. Fluid Mech., *175,* 157–181.

Chavanis, P. H. and J. Sommeria. 1996. Classification of self-organized structures in 2-D turbulence. The case of a bounded domain. J. Fluid Mech., *314,* 267–299.

Cummins, P. F. 1992. Inertial gyres in decaying and forced geostrophic turbulence. J. Mar. Res., *50,* 545–566.

Cummins, P. F. and G. Holloway. 1994. On eddy-topographic stress representation. J. Phys. Oceanogr., *24,* 700–706.

Eby, M. and G. Holloway. 1994. Sensitivity of a large scale ocean model to a parameterization of topographic stress. J. Phys. Oceanogr., *24,* 2577–2588.

Errico, R. M. 1984. The statistical equilibrium solution of a primitive-equation model. Tellus, *36*(A), 42–51.

Fofonoff, N. P. 1954. Steady flow in a frictionless homogeneous ocean. J. Mar. Res., *13,* 254–262.

Gent, P. R. 1993. The energetically consistent shallow-water equations. J. Atmos. Sci., *50,* 1323–1325.

Griffa, A. and S. Castellari. 1991. Nonlinear general circulation of an ocean model driven by wind with a stochastic component. J. Mar. Res., *49,* 53–73.

Griffa, A. and R. Salmon. 1989. Wind-driven ocean circulation and equilibrium statistical mechanics. J. Mar. Res., *47,* 457–492.

Holloway, G. 1986. Eddies, waves, circulation and mixing: Statistical geofluid mechanics. Ann. Rev. Fluid Mech., *18,* 91–147.

—— 1992. Representing topographic stress for large scale ocean models. J. Phys. Oceanogr., *22,* 1033–1046.

Ierley, G. 1990. Boundary layers in the general ocean circulation. Annu. Rev. Fluid. Mech., *22,* 111–142.

Marshall, J. C. 1984. Eddy-mean flow interaction in a barotropic ocean model. Q.J.R. Meteorol. Soc., *110,* 573–590.

Miller, J. 1990. Statistical mechanics of Euler equations in two dimensions. Phys. Rev. Lett., *65,* 2137–2140.

Robert, R. and J. Sommeria. 1991. Statistical equilibrium states for two-dimensional flows. J. Fluid Mech., *229,* 291–310.

Roubicek, A., E. Chassignet and A. Griffa. 1995. Topographic stress parameterization in a primitive equation ocean model: Impact on mid-latitude jet separation, *in* Flow-Topography, Proceedings of Aha Hliko'a Hawaiian Winter Workshop, University of Hawaii, 1995. P. Muller and G. Holloway, eds., 239–252.

Sadourny, R. 1975. The dynamics of finite-difference models of the shallow-water equations. J. Atmos. Sci., *32*, 680–689.

Salmon, R. 1982a. The shape of the main thermocline. J. Phys. Oceanogr., *12*, 1458–1479.

——— 1982b. Geostrophic turbulence, *in* Topics in Ocean Physics, A. R. Osborne and P. M. Rizzoli, eds., North-Holland, Amsterdam, 30–78.

Salmon, R., G. Holloway and M. C. Hendershott. 1976. The equilibrium statistical mechanics of simple quasigeostrophic models. J. Fluid Mech., *75*, 691–703.

Vallis, G. K. and M. E. Maltrud. 1993. Generation of mean flows and jets on a beta plane and over topography. J. Phys. Oceanogr., *23*, 1346–1362.

Wang, J. and G. K. Vallis. 1994. Emergence of Fofonoff states in inviscid and viscous ocean circulation models. J. Mar. Res., *52*, 83–127.

Weichman, P. B. 1993. Statistical mechanics, Euler's equation and Jupiter's red spot, *in* Nonlinear Waves and Weak Turbulence with Applications in Oceanography and Condensed Matter Physics, N. Fitzmaurics, D. Gurarie, F. Mc Caughan and W. A. Woyczynski eds., Birkhauser, Boston, MA, 239–309.